



Low-Temperature Sintering Characteristics of Ag-Based Complex Inks Using Transient Melting and Joining of Sn–58Bi Nanoparticles

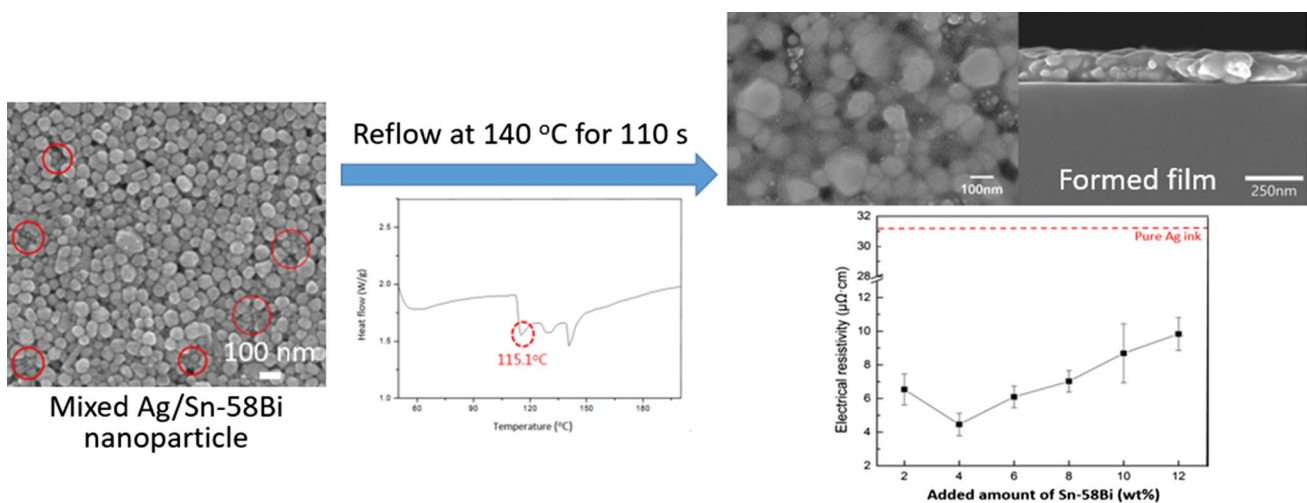
Woo Lim Choi¹ · Jong-Hyun Lee¹

Received: 28 March 2019 / Accepted: 6 May 2019
© The Korean Institute of Metals and Materials 2019

Abstract

A novel complex ink was fabricated by mixing Sn–58Bi nanoparticles with a commercial conductive ink containing Ag nanoparticles and then sintered rapidly for 110 s at 140 °C in air using a conveyor-type reflow furnace. Sn–58Bi nanoparticles smaller than 15 nm wetted on the neighboring Ag nanoparticles immediately after melting at temperatures lower than their melting point, and hence, acted as transient liquid-phase binders. The composite film sintered with 4 wt% Sn–58Bi exhibited stability and a low electrical resistivity of 4.46 $\mu\Omega$ cm, and hence, was found to be compatible with low-cost flexible films.

Graphical Abstract



Keywords Sintering · Electrical resistivity · Thin films · Nanostructure · Complex ink

1 Introduction

With the rapid development in the field of printed electronics (for smart manufacturing), Ag inks have gained immense attention for the fabrication of conductive patterns

or electrodes on various non-conductive surfaces directly [1–4]. The use of conducting inks is imperative to achieve fine patterning (by a combination of techniques such as ink-jet printing or off-set printing) [5–7]. Moreover, Ag inks do not cause oxidation of sintered films even after heating in air, improving their electrical conductivity [8, 9].

However, commercial Ag nanoparticle inks require high sintering temperatures and a long sintering duration [10–12], which limit their widespread use. The sintering temperature of Ag inks is as high as 150–300 °C [13]. This high sintering temperature limits their applications in various films,

✉ Jong-Hyun Lee
pljh@snut.ac.kr

¹ Department of Materials Science and Engineering,
Seoul National University of Science and Technology,
Seoul 01811, Republic of Korea

modules, and processes. By reducing the sintering temperature of Ag inks by 10 °C, low-cost materials such as polycarbonate or polyethylene terephthalate films can be used easily as flexible substrates. Therefore, the sintering characteristics of Ag inks at ~140 °C are the most crucial factors affecting the mass production of flexible electronic devices. Generally, Ag inks require long sintering durations of 30–60 min; however, this time is strongly dependent on the sintering temperature and particle size [14]. This is because the sintering of Ag particles is attributed to simply a solid-state diffusion mechanism [15, 16]. However, the solid-state sintering mechanism can be transformed into a liquid-phase sintering mechanism (extraordinarily rapidly) by adding an optimum amount of metal nanoparticles having a melting point lower than the sintering temperature [17]. The enhanced sinterability can increase the productivity of smart manufacturing and significantly reduce the length of the continuous curing line when a conveyor system is used. In addition, the high cost of Ag inks can be reduced by adding metal nanoparticles. However, the excessive addition of low-melting-point particles to induce liquid-phase sintering can significantly deteriorate the shape of the sintered film. For example, it can result in the formation of round-shaped edges in a sintered film by a downward flow due to the generation of the liquid-phase [18]. Thus, it is imperative to add metal particles acting as transient liquid-phase binders that exist in the liquid phase only for a certain duration after melting.

Therefore, in this study, we performed low-temperature (140 °C, in air) sintering of complex inks consisting of Ag and Sn–58(wt%) Bi nanoparticles. The average size of the Sn–58Bi nanoparticles was approximately 15 nm. The Sn–58Bi particles that were smaller than the average size got melted at temperatures lower than their equilibrium melting point (138 °C). This could be attributed to the melting-point depression phenomenon caused by the Gibbs–Thompson effect [19–21]. Concurrently, the wetting and adhesion of the molten Sn–58Bi nanoparticles to the Ag nanoparticles could induce their rapid solidification because of an instant increase in their radius of curvature due to the shape transformation [17].

2 Experimental Procedures

Sn–58Bi nanoparticles fabricated using the modified direct current-arc (DCA) method [20, 21] were purchased from Able Metal Co. Ltd. These Sn–58Bi nanoparticles were then dispersed in different alcohol solvents to form Sn–58Bi inks. DGP 40LT-15C Ag ink (ANP) was used as the base ink to fabricate the complex ink. The Sn–58Bi inks and a small amount (0.003 and 0.006 g) of flux (Indalloy Flux#1, Indium Corporation) were added to the Ag ink, and the resulting mixture was mixed rapidly for 2 min using a homogenizer

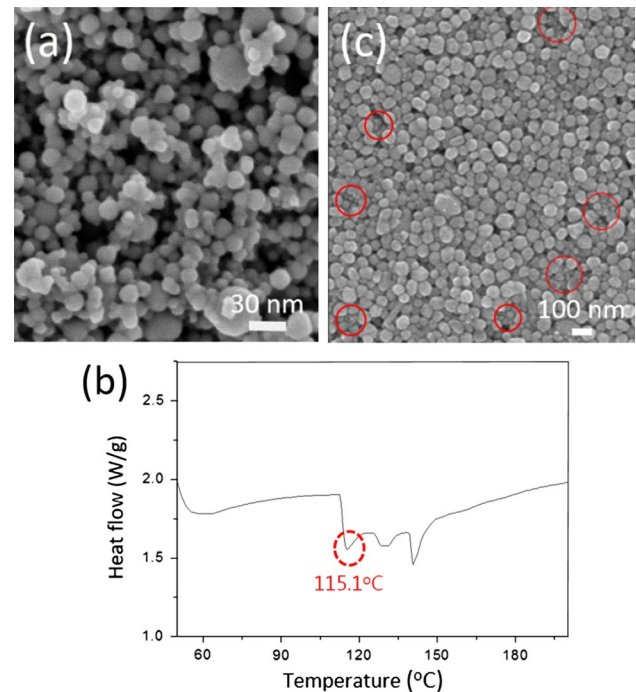


Fig. 1 a SEM image and b TG-DSC curve of the Sn–58Bi nanoparticles used in this study. c SEM image of the Ag ink containing the Sn–58Bi nanoparticles

(Pro-200, Pro Scientific). Complex inks with different Sn–58Bi inks prepared with different solvents and Sn–58Bi nanoparticle amounts were prepared.

The prepared complex ink (80 mL) was coated on a 10 mm × 10 mm Si chip using a spin coater (Spin-1200D, Midas System). The spin coating process involved three steps. The first and second steps were conducted for 5 s at 500 and 1000 rpm, respectively. The third step was performed for 30 s at 2000 rpm. The coatings were annealed

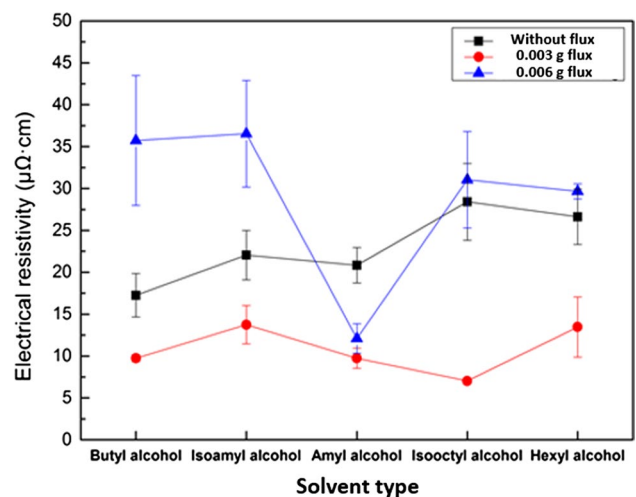
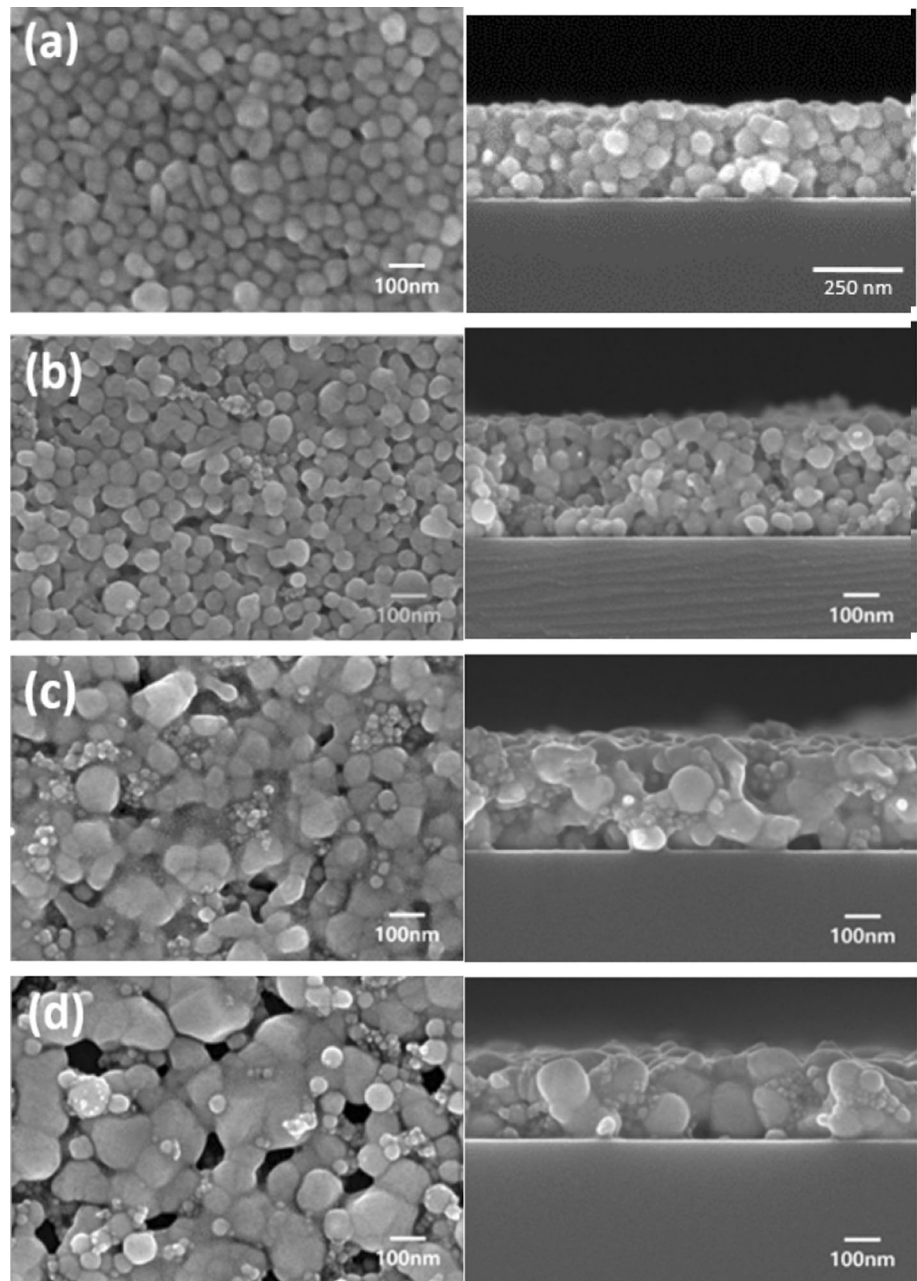


Fig. 2 Electrical resistivity of the Ag/20 wt% Sn–58Bi complex ink with different solvents and flux contents

Fig. 3 Surface and cross-sectional SEM images of the films sintered under different conditions: **a** pure Ag and amyloalcohol-based Ag/20 wt% Sn–58Bi complex inks **b** without flux and with **c** 0.003 g and **d** 0.006 g flux



in air using a conveyor-type reflow furnace (T-960, Puhui Electric Technology). The temperature profiles of the complex inks revealed that they showed a peak temperature of 140 °C, holding time of 110 s at the peak temperature, and total processing time of 5 min, which is similar to a normal reflow profile.

The thermal characteristics of the Sn–58Bi nanoparticles used in this study were investigated by thermogravimetric-differential scanning calorimetry (TG-DSC, Q20, TA Instrument installed in KBSI PH407 Pusan) at a heating rate of 10 °C/min. The shape and size of the Sn–58Bi nanoparticles

and surface and cross-sectional microstructures of the sintered composite films were examined via a field emission-scanning electron microscope (HR FE-SEM, SU-8010, Hitachi). The electrical resistivities of the surfaces of the sintered films were measured by the four-point probe method (1-mm interval) using a source meter (2400, Keithley Instruments). The resistivity, ρ , of the films was calculated using the following equation: $\rho = Rct$, where R , c , and t are the electrical sheet resistance, correction factor, and film thickness, respectively. Each sample was measured 40 times, and the average resistivity values were noted.

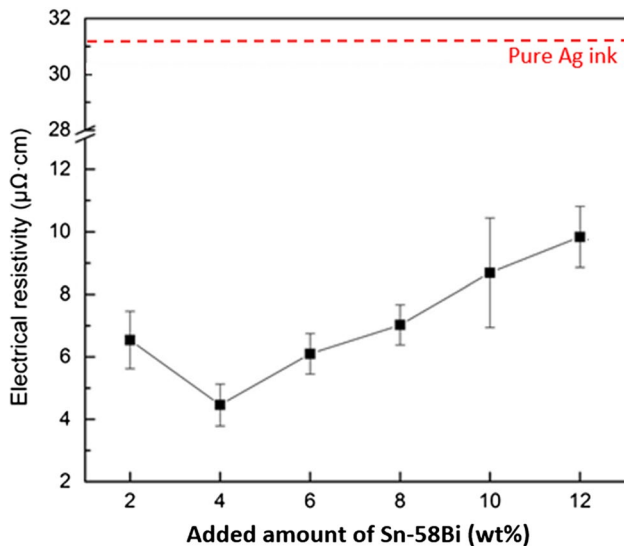


Fig. 4 Electrical resistivity of the Ag-based composite films sintered for 110 s at 140 °C as a function of the Sn-58Bi content

3 Results and Discussion

Figure 1a, b show the SEM image and TG-DSC curves, respectively, of the Sn-58Bi nanoparticles used in this study. Although the particles have a size range of 5–65 nm, most of them are smaller than 15 nm. The smaller particles in the range exhibit melting-point depression induced by the Gibbs–Thompson effect. The Sn-58Bi nanoparticles show the first endothermic peak at 115.1 °C, which is 22.9 °C lower than their melting point (138 °C). This demonstrates the melting-point depression of the nanoparticles. Because the degree of melting-point depression of a material is inversely proportional to its particle size, the nanoparticles display another endothermic peak at around 130 °C before reaching the equilibrium melting point. Figure 1c shows the SEM image of the Ag ink containing the Sn-58Bi nanoparticles. Although the Sn-58Bi particles are locally aggregated, they randomly exist between the larger Ag particles (30–100 nm) after the mixing.

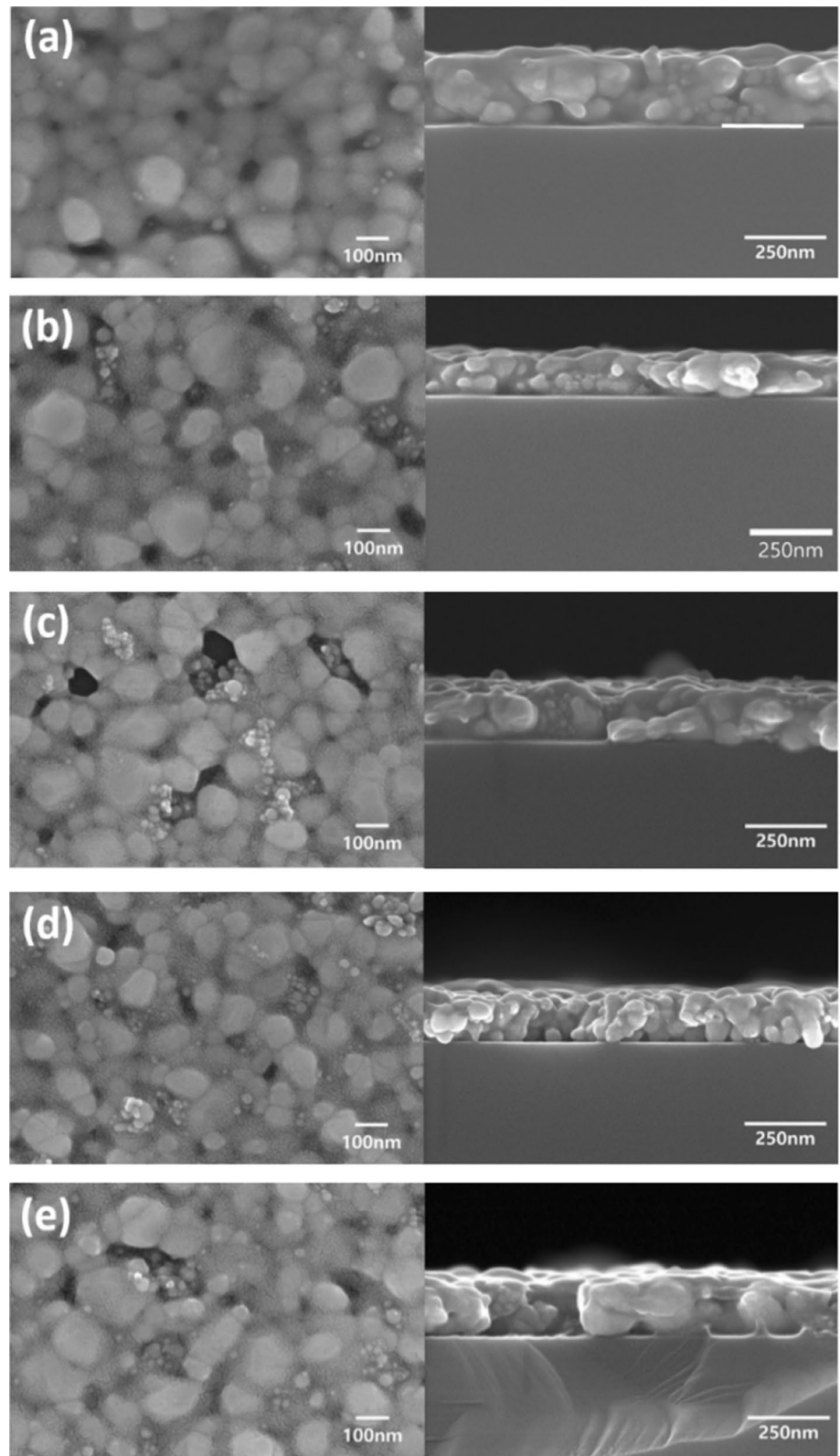
Figure 2 shows the electrical resistivities of the Ag/20 wt% Sn-58Bi complex inks prepared with different solvents and flux contents. The solvent type significantly affects the final resistance of Sn-58Bi. Sn-58Bi nanoparticles prepared in amyl alcohol generally show a low resistivity regardless of the flux content. The Sn-58Bi particles prepared using different solvents via a modified DAC method exhibit different qualities and degrees of surface oxidation. Moreover, the boiling point of the solvent significantly affects the resistivity of the sintered films. In the case of the composite films formed without a flux, the resistivity increases with an increase in the boiling point of the solvent. The solvents having high boiling points remain inside the film for a long

time without the vaporization during heating, which hinders the sintering process. The oxide decomposition ability of the flux changes significantly with the use of different solvents. Because of this variation, the sintered films show different characteristics. In the amyl-alcohol-based complex ink, a slight flux addition of 0.003 g results in a significant decrease in the resistivity to 9.73 μΩ cm, indicating the wetting and sintering of the molten Sn-58Bi particles on the Ag particles by the decomposition of tin oxide. However, the resistivity decreases with a further increase in the flux.

This can be attributed to the difference in the microstructures of the films (Fig. 3). Figure 3a shows the surface and cross-sectional SEM images of the pure Ag ink. The Ag grains in this case are found to be similar to those in the original Ag nanoparticles, indicating insufficient sintering owing to the low processing temperature and short sintering time. The average resistivity of the film is 31.2 μΩ cm. Contrastingly, the film with 20 wt% Sn-58Bi without any added flux (Fig. 3b) shows agglomerated grains (locally among the Sn-58Bi nanoparticles) (clearer in the cross-sectional image). The cross-sectional image of this film exhibits microstructures linking between Ag particles, unlike in the case of the pure Ag film. This indicates that amyl alcohol plays the role of the flux. The addition of a small amount of flux (0.003 g) significantly enhances the connectivity between the Ag particles, resulting in the melting of the Sn-58Bi nanoparticles, despite the presence of locally agglomerated Sn-58Bi nanoparticles (Fig. 3c). Thus, large grains are formed. Moreover, an opaque flux residue can be clearly observed between the grown particles because no cleaning process is performed after the sintering. The grain size increases with an increase in the flux (Fig. 3d), despite the agglomeration of the Sn-58Bi nanoparticles. Nevertheless, the unexpected increase in the resistivity can be explained by the increase in the flux residue between the grains, which significantly impedes the electron transfer, thereby increasing the electrical resistance of the film. Furthermore, the rapid sintering by the molten Sn-58Bi nanoparticles generates numerous large voids at the surface, which inhibit the transfer of electrons. This also might cause an increase in the resistance of the film. Despite the melting of the Sn-58Bi nanoparticles, the height of the film does not decrease significantly (because the collapse of the film structure did not progress) (Fig. 3c, d). This indicates that the Sn-58Bi nanoparticles show transient melting behavior.

The electrical resistivity of the composite film sintered for 110 s at 140 °C with 0.003 g flux as a function of the Sn-58Bi content is shown in Fig. 4. Because numerous Sn-58Bi nanoparticles did not participate in the sintering process (Fig. 3), only small Sn-58Bi amounts are considered. In the case of pure Ag ink, the treatment temperature and time are not sufficient for inducing the sintering behavior. The resistivity of the pure Ag film decreases rapidly

Fig. 5 **a** Surface and **b** cross-sectional SEM images of the Ag-based composite films with different Sn–58Bi amounts: **a** 2, **b** 4, **c** 6, **d** 8, and **e** 12 wt%



from 31.2 to 6.54 $\mu\Omega$ cm with the addition of only 2 wt% Sn–58Bi. With a further increase in the Sn–58Bi content reaching up to 4 wt%, the resistivity of the pure Ag film

decreases to 4.46 $\mu\Omega$ cm. However, the resistivity increases with an increase in the Sn–58Bi content to reach beyond 6 wt%. In summary, the complex ink sintered films showed

a significantly reduced electrical resistivity as compared to the pure Ag ink sintered film. The optimum Sn–58Bi doping amount is found to be 4 wt% or 7.8 vol%, which is significantly lower than the vacancy volume (26 vol%) estimated by the close-packing model of hard spheres [22]. To identify the reason for this, microstructural analyses were performed.

The surface and cross-sectional microstructures of the films are observed and shown in Fig. 5. The film with 2 wt% Sn–58Bi (Fig. 5a) shows many grains larger than those in the original Ag particles. Though grains with sizes comparable to the size of Ag particles are also observed, Sn–58Bi aggregates can be barely observed. However, in the case of the film with 4 wt% Sn–58Bi (Fig. 5b), large grains are observed along with some Sn–58Bi aggregates. With the increase in the Sn–58Bi content to 6 wt% (Fig. 5c), the fraction of the Sn–58Bi aggregates increases significantly, whereas the grain growth does not proceed remarkably. A similar tendency is exhibited by the Ag/8 wt% Sn–58Bi film (Fig. 5d). The fraction of large grains increases significantly with the increase in the Sn–58Bi content to 12 wt% (Fig. 5e). The number of Sn–58Bi aggregates also increases. These results suggest that the presence of numerous Sn–58Bi aggregates increases the electrical resistance of the Ag ink sintered films because of the poor connectivity between the grains. If all the added Sn–58Bi nanoparticles were less than 15 nm in size and perfectly dispersed, the lowest resistivity might have been obtained when the Sn–58Bi content approached 26 vol%. However, the size distribution of the Sn–58Bi nanoparticles and their imperfect mixing [owing to the quality of the initially aggregated state (Fig. 1a)] reduced the optimum Sn–58Bi addition content. The perfect dispersion of the Sn–58Bi nanoparticles was important. Although, Sn–58Bi nanoparticles smaller than 15 nm could melt at temperatures lower than the equilibrium melting point, they transformed into larger ones by coarsening and solidifying (on contact with the neighboring Sn–58Bi nanoparticles) because of the loss of their melting-point depression ability. This behaviour did not contribute to the connection between the Ag particles. The Sn–58Bi nanoparticles did not act as transient liquid-phase binders and increased the electrical resistivity of the sintered films by creating gaps on the surface of the Ag particles.

4 Conclusion

The sinterability of pure Ag ink increased significantly with the addition of Sn–58Bi nanoparticles which acted as the transient liquid-phase binder. After sintering for 110 s at 140 °C

in air using a conveyor-type reflow furnace, the electrical resistivity of the pure Ag ink film decreased rapidly from 31.2 to 4.46 $\mu\Omega$ cm. In addition, the sintered film maintained the required form without the significant collapse of a film structure.

References

1. A. Kosmala, R. Wright, Q. Zhang, P. Kirby, *Mater. Chem. Phys.* **129**, 1075 (2011)
2. T.H.J. van Osch, J. Perelaer, A.W.M. de Laat, U.S. Schubert, *Adv. Mater.* **20**, 343 (2008)
3. M. Singh, H.M. Haverinen, P. Dhagat, G.E. Jabbour, *Adv. Mater.* **22**, 673 (2010)
4. S. Gamerith, A. Klug, H. Scheiber, U. Scherf, E. Moderegger, E.J.W. List, *Adv. Funct. Mater.* **17**, 3111 (2007)
5. K. Murata, J. Matsumoto, A. Tezuka, Y. Matsuba, H. Yokoyama, *Microsyst. Technol.* **12**, 2 (2005)
6. K. Cheng, M.H. Yang, W.W.W. Chiu, C.Y. Huang, J. Chang, T.F. Ying, Y. Yang, *Macromol. Rapid Commun.* **26**, 247 (2005)
7. D. Kang, E. Lee, H. Kim, Y.M. Choi, S. Lee, I. Kim, D. Yoon, J. Jo, B. Kim, T.M. Lee, *J. Appl. Phys.* **115**, 234908 (2014)
8. S. Merilampi, T. LaineMa, P. Ruuskanen, *Microelectron. Reliab.* **49**, 782 (2009)
9. S.B. Walker, J.A. Lewis, *J. Am. Chem. Soc.* **134**, 1419 (2012)
10. J. Perelaer, M. Klokkenburg, C.E. Hendriks, U.S. Schubert, *Adv. Mater.* **21**, 4830 (2009)
11. J. Perelaer, A.W.M. de Laat, C.E. Hendriks, U.S. Schubert, *J. Mater. Chem.* **18**, 3209 (2008)
12. S. Magdassi, M. Grouchko, O. Berezin, A. Kamyshny, *ACS Nano* **4**, 1943 (2010)
13. C.I. Yeo, J.H. Kwon, S.J. Jang, Y.T. Lee, *Opt. Express* **20**, 19554 (2012)
14. S. Lehtimäki, M. Li, J. Salomaa, J. Porhonen, A. Kalanti, S. Tuukkanen, P. Heljo, K. Halonen, D. Lupo, *Int. J. Electr. Power Energy Syst.* **58**, 42 (2014)
15. T.G. Lei, J.N. Calata, G.-Q. Lu, X. Chen, S. Luo, *I.E.E.E. Trans. Compon. Packag. Technol.* **33**, 98 (2010)
16. K.S. Siow, *J. Alloys Compd.* **154**, 6 (2012)
17. Y.M. Shin, H.J. Kim, S.P. Jang, J.H. Lee, *J. Electron. Mater.* **43**, 3372 (2014)
18. W.D. Kingery, *J. Appl. Phys.* **30**, 301 (1959)
19. F. Frongia, M. Piloni, A. Scano, A. Ardu, C. Cannas, A. Musinu, G. Borzone, S. Delsante, R. Novakovic, G. Ennas, *J. Alloys Compd.* **623**, 7 (2015)
20. Y. Gao, C. Zou, B. Yang, Q. Zhal, J. Liu, E. Zhuravlev, C. Schick, *J. Alloys Compd.* **484**, 777 (2009)
21. J. Zhao, Y. Gao, W. Zhang, T. Song, Q. Zhai, *J. Mater. Sci.: Mater. Electron.* **23**, 2221 (2012)
22. A.G. Tefera, M.D. Mochena, E. Johnson, J. Dickerson, *J. Appl. Phys.* **116**, 104301 (2014)

Publisher's Note Springer Nature remains neutral with regard to jurisdictional claims in published maps and institutional affiliations.